The Infrared Medium-deep Survey. IV. The Low Eddington Ratio of A Faint Quasar at $z \sim 6$: Not Every Supermassive Black Hole is Growing Fast in the Early Universe

Yongjung Kim[1,2] , Myungshin Im[1,2] , Yiseul Jeon[1,3] , Minjin Kim[4,5] , Minhee Hyun[1,2], Dohyeong Kim[1,2], Jae-Woo Kim[4] ,
Yoon Chan Taak[1,2], Yongmin Yoon[1,2], Changsu Choi[1,2], Jueun Hong[1,2], Hyunsung David Jun[1,6], Marios Karouzos[7] ,
Duho Kim[1,8] , Ji Hoon Kim[9] , Seong-Kook Lee[1,2] , Soojong Pak[10] , and Won-Kee Park[4]

[1] Center for the Exploration of the Origin of the Universe (CEOU), Building 45, Seoul National University, 1 Gwanak-ro, Gwanak-gu, Seoul 08826, Republic of Korea; yjkim@astro.snu.ac.kr, mim@astro.snu.ac.kr
[2] Astronomy Program, FPRD, Department of Physics & Astronomy, Seoul National University, 1 Gwanak-ro, Gwanak-gu, Seoul 08826, Republic of Korea
[3] LOCOOP, Inc., 311-1, 108 Gasandigital2-ro, Geumcheon-gu, Seoul, Republic of korea
[4] Korea Astronomy and Space Science Institute, Daejeon 34055, Republic of Korea
[5] University of Science and Technology, Daejeon 305-350, Republic of Korea
[6] Korea Institute for Advanced Study, 85 Hoegi-ro, Dongdaemun-gu, Seoul 02455, Republic of korea
[7] Nature Astronomy, Springer Nature, 4 Crinan street, London N1 9XW, UK
[8] Arizona State University, School of Earth and Space Exploration, P.O. Box 871404, Tempe, AZ 85287-1404, USA
[9] Subaru Telescope, National Astronomical Observatory of Japan, 650 North A'ohoku Place, Hilo, HI 96720, USA
[10] School of Space Research, Kyung Hee University, 1732 Deogyeong-daero, Giheung-gu, Yongin-si, Gyeonggi-do 17104, Republic of Korea
Received 2017 May 29; revised 2018 February 5; accepted 2018 February 5; published 2018 March 16

Abstract

To date, most of the luminous quasars known at $z \sim 6$ have been found to be in maximal accretion with the Eddington ratios, $\lambda_{\mathrm{Edd}} \sim 1$, suggesting enhanced nuclear activities in the early universe. However, this may not be the whole picture of supermassive black hole (SMBH) growth, since previous studies have not reached faint quasars that are more likely to harbor SMBHs with low λ_{Edd}. To gain a better understanding of the accretion activities in quasars in the early universe, we obtained a deep near-infrared (NIR) spectrum of a quasar, IMS J220417.92+011144.8 (hereafter IMS J2204+0112), one of the faintest quasars that has been identified at $z \sim 6$. From the redshifted C IV $\lambda 1549$ emission line in the NIR spectrum, we find that IMS J2204+0112 harbors a SMBH with a solar mass of about a billion and $\lambda_{\mathrm{Edd}} \sim 0.1$, but with a large uncertainty in both quantities (0.41 dex). IMS J2204+0112 has one of the lowest Eddington ratios among quasars at $z \sim 6$, but a common value among quasars at $z \sim 2$. Its low λ_{Edd} can be explained with two scenarios; the SMBH growth from a stellar-mass black hole through short-duration super-Eddington accretion events or from a massive black hole seed ($\sim 10^5 \, M_\odot$) with Eddington-limited accretion. NIR spectra of more faint quasars are needed to better understand the accretion activities of SMBHs at $z \sim 6$.

Key words: cosmology: observations – galaxies: active – galaxies: high-redshift – galaxies: nuclei – quasars: emission lines – quasars: supermassive black holes

1. Introduction

Since the first discovery of a quasar in 1960s, more than 400,000 quasars have been discovered by numerous surveys (e.g., Schmidt & Green 1983; Hewett et al. 1995; Boyle et al. 2000; Im et al. 2007; Lee et al. 2008; Shen et al. 2008, 2011; Flesch 2015; Jeon et al. 2017; Pâris et al. 2017). Among them, about 100 quasars have been identified at $z \gtrsim 6$ (Fan et al. 2000, 2006; Goto 2006; Jiang et al. 2009, 2016; Willott et al. 2010b; Mortlock et al. 2011; Venemans et al. 2013, 2015a, 2015b; Bañados et al. 2014, 2016, 2018; Kashikawa et al. 2015; Kim et al. 2015; Wu et al. 2015; Matsuoka et al. 2016, 2018; Mazzucchelli et al. 2017). Compared to quasars at lower redshifts, these high-redshift quasars show no remarkable evolution in UV/optical spectral shapes (Fan et al. 2006; Jun et al. 2015), but a larger fraction of them is found to be dust-poor compared to their low-redshift counterparts, a possible indication that high-redshift quasars are rapidly evolving (Jiang et al. 2010; Jun & Im 2013).

Using a black hole (BH) mass estimator that assumes Doppler broadening of virialized gas as the dominant cause for the broad emission lines of quasars (e.g., see Kim et al. 2010; Jun et al. 2015), the black hole masses (M_{BH}) of few tens of high-redshift quasars are found to be $10^{8-10} \, M_\odot$ (Jiang et al. 2007; Kurk et al. 2007, 2009; Willott et al. 2010a; Mortlock

et al. 2011; Shen et al. 2011; Jun et al. 2015; Venemans et al. 2015a; Wu et al. 2015). Interestingly, the existence of supermassive black holes (SMBHs) in such an early universe poses a theoretical challenge for the following reason.

The SMBH mass at a given time t ($M_{\mathrm{BH}}(t)$) can be expressed as,

$$M_{\mathrm{BH}}(t) = M_{\mathrm{BH},0} \times \exp\left(\dot{m} f_{\mathrm{Duty}} (1 - \epsilon) \frac{t - t_0}{t_{\mathrm{Edd}}}\right), \quad (1)$$

where $\dot{m}$ is the mass accretion rate normalized by Eddington mass accretion (see Watarai et al. 2001; Volonteri et al. 2015), $t_{\mathrm{Edd}} = 450$ Myr, ϵ is the radiation efficiency, f_{Duty} is the duty cycle, $M_{\mathrm{BH},0}$ is the seed BH mass, and t_0 is the time when the seed BH started to grow. For a standard disk model with Eddington-limited accretion, $\dot{m} = \lambda_{\mathrm{Edd}}/\epsilon = (L_{\mathrm{bol}}/L_{\mathrm{Edd}})/\epsilon$, where λ_{Edd} is the Eddington ratio, L_{bol} is the bolometric luminosity, and L_{Edd} is the Eddington luminosity ($L_{\mathrm{Edd}} = 1.26 \times 10^{38} \, (M_{\mathrm{BH}}/M_\odot)$ in erg s^{-1}). Adopting a typical value of $\epsilon = 0.1$, even with a continuous maximal accretion at $\lambda_{\mathrm{Edd}} = 1$, it requires about ~ 0.8 Gyr for a stellar-mass BH with $M_{\mathrm{BH},0} = 100 \, M_\odot$ to grow into $10^9 \, M_\odot$. The age of the universe is only 0.94 Gyr at $z = 6$ and 0.48 Gyr at $z = 10$

(a plausible redshift for a stellar-mass BH to form), so the creation of a $10^9\,M_\odot$ BH is nearly impossible especially when we also consider feedbacks from star formation and AGN activity that hinder the continuous Eddington-limited accretion (Pelupessy et al. 2007; Alvarez et al. 2009; Milosavljević et al. 2009; Jeon et al. 2012; Park & Ricotti 2012; Johnson et al. 2013). To solve this problem, super-Eddington accretion ($\lambda_{\rm Edd} > 1$) of stellar-mass BHs (e.g., Volonteri & Rees 2005; Wyithe & Loeb 2012; Madau et al. 2014), and BH growth from massive seed BHs with $10^{4-6}\,M_\odot$ are introduced (e.g., Bromm & Loeb 2003; Begelman et al. 2006; Lodato & Natarajan 2006; Johnson et al. 2013).

Testing these different SMBH growth scenarios requires understanding Eddington ratios of high-redshift quasars. So far, the Eddington ratios are measured for about 20 luminous $z \sim 6$ quasars (bolometric luminosity, $L_{\rm bol} \gtrsim 10^{47}\,{\rm erg\,s^{-1}}$) and the values are found to be at $\lambda_{\rm Edd} \sim 1$ (e.g., see Willott et al. 2010a; Jun et al. 2015; Wu et al. 2015) in contrast to $\lambda_{\rm Edd} \sim 0.1$ of their counterparts at lower redshifts (Richards et al. 2006; Shen et al. 2011; Trakhtenbrot & Netzer 2012). The predominantly Eddington-limited accretion of SMBHs at high redshift might be in line with the rapid accretion scenario in the models that allow stellar-mass seed BHs (e.g., see Alexander & Hickox 2012; Volonteri 2012; Johnson et al. 2013 and references therein).

However, previous studies have been limited mostly to luminous quasars that are likely to be high $\lambda_{\rm Edd}$ objects. Therefore, the suggestion that high-redshift quasars are rapidly growing could be a result of this kind of bias. To avoid the bias, Willott et al. (2010a) tried to infer the intrinsic $\lambda_{\rm Edd}$ distribution from the observed $\lambda_{\rm Edd}$ distribution of 17 luminous quasars at $z \sim 6$ with an assumption that the distribution follows a lognormal form. According to their analysis, the peak of the intrinsic $\lambda_{\rm Edd}$ distribution of $z \sim 6$ quasars is $\log(\lambda_{\rm Edd}) = -0.22$, in comparison to the observed peak at $\log(\lambda_{\rm Edd}) \sim 0.03$. This result indicates that there should be more quasars with $\lambda_{\rm Edd} < 1$ if fainter luminosity quasars are explored, but it still implies nearly Eddington-limited accretion for most $z \sim 6$ quasars. However, recent studies of $z \sim 6.5$ quasars (De Rosa et al. 2014; Venemans et al. 2015a; Mazzucchelli et al. 2017) suggested that there are a few $10^{46.5-47}\,{\rm erg\,s^{-1}}$ luminous quasars with $M_{\rm BH} > 10^{9.0}\,M_\odot$, and the average $\log(\lambda_{\rm Edd})$ of 15 $z \sim 6.5$ quasars is 0.39, which is comparable to their low-redshift counterparts (Mazzucchelli et al. 2017), implying that the derived intrinsic $\lambda_{\rm Edd}$ distribution of Willott et al. (2010a) is biased toward high $\lambda_{\rm Edd}$. Also, a possible positive correlation of $L_{\rm bol}$ and $\lambda_{\rm Edd}$ for low-redshift quasars (Shen et al. 2008, 2011; Lusso et al. 2012) may lead to the same conclusion. Since the majority of quasars at high redshift are faint, as implied by the quasar luminosity function (Willott et al. 2010b; Giallongo et al. 2015; Kashikawa et al. 2015; Kim et al. 2015), these limited quasar sample cannot truly represent the whole quasar population at $z \sim 6$, if $z \sim 6$ quasars have such a $L_{\rm bol} - \lambda_{\rm Edd}$ relation like their low-redshift counterparts.

Thanks to the recent wide-area deep surveys, new light can be shed on the accretion activities of high-redshift quasars. Now, dozens of faint $z \sim 6$ quasars are spectroscopically identified that have absolute magnitudes at a rest-frame 1450 Å of $M_{1450} > -24$ mag (Kashikawa et al. 2015; Kim et al. 2015; Matsuoka et al. 2016, 2018). These faint quasars can possibly represent the population of low $\lambda_{\rm Edd}$ SMBHs. Therefore, to really see how fast high-redshift quasars are growing, it is important to measure their $M_{\rm BH}$ and $\lambda_{\rm Edd}$ values. So far, little has been done to characterize these faint quasars at high redshift, but deep NIR spectroscopy with sensitive spectrographs should be able to reveal their $M_{\rm BH}$ and $\lambda_{\rm Edd}$ one by one.

In this paper, we present the first NIR spectroscopic observation of IMS J2204+0112 (Kim et al. 2015), one of the faintest $z \sim 6$ quasars discovered so far from the Infrared Medium-deep Survey (M. Im et al. 2018, in preparation). We describe the observation and the data analysis in Section 2. We present the quasar's spectral properties that are obtained through continuum/line-fitting in Section 3. We present the $M_{\rm BH}$ and $\lambda_{\rm Edd}$ values of IMS J2204+0112 in Section 4. The implications of our results about the growth SMBHs in the early universe are discussed in Section 5. We adopt $\Omega_m = 0.3$, $\Omega_\Lambda = 0.7$, and $H_0 = 70\,{\rm km\,s^{-1}\,Mpc^{-1}}$ of a concordance cosmology that has been supported by observations in the past decades (e.g., Im et al. 1997).

2. Observation and Data Analysis

The NIR spectroscopic observation of IMS J2204+0112 was carried out with the Folded-port InfraRed Echellette (FIRE) mounted on the Magellan/Baade 6.5 m telescope at the Las Campanas Observatory in Chile. The observation aimed to detect the redshifted C IV line, a common $M_{\rm BH}$ estimator (Vestergaard & Peterson 2006; Jun et al. 2015). Mg II is another, possibly better choice for $M_{\rm BH}$ measurement (Shen et al. 2011; Ho et al. 2012; Jun et al. 2015), but we opted for the C IV line due to the observational difficulty of detecting Mg II at longer wavelengths. We observed the target with the high-throughput prism mode (or long-slit mode) on 2015 September 12th and 13th. The data were taken with a $1\farcs0$ slit, which gives a spectral resolution in the J-band (R_J) of 500, corresponding to a resolution of $\sim 600\,{\rm km\,s^{-1}}$. The single exposure time for each frame was set at 908.8 s with the Sample-Up-The-Ramp readout mode, which reads out the detector continuously during exposure. This kind of long exposure in NIR observation makes the long-wavelength region ($\lambda > 12000$ Å) saturated, but enables us to obtain sufficient signals (S/N $\gtrsim 3$ over a resolution element) for a continuum at short wavelengths ($\lambda < 12000$ Å). We took 26 frames for IMS J2204+0112, but only 20 frames taken under good weather conditions (seeing $\lesssim 1\farcs0$) were used for the data analysis, giving a net exposure time of 5.05 hr.

Although the data were obtained through a nodding observation (i.e., ABBA offset), varying seeing conditions during the observing run with long exposures generated unstable sky-lines on the spectra. This made it difficult to eliminate the sky-lines directly by subtracting raw frames from each other. Thus, we processed the spectra one by one, using the IRAF package (Tody 1993). Saturated regions ($\lambda > 12000$ Å) were trimmed, and then we performed the bias subtraction and the flat-fielding. The wavelength solutions were derived from the NeAr arc frames. In order to eliminate sky-lines, we subtracted the median value of background pixels surrounding the target in the spatial direction from the wavelength-calibrated, reduced spectrum, giving us clear sky-subtracted images around the target. After combining the images, we extracted the spectrum with a $1\farcs0$ aperture. Telluric correction with a standard star (HD 216807) was applied to the extracted 1D spectrum. We adjusted the flux scale of
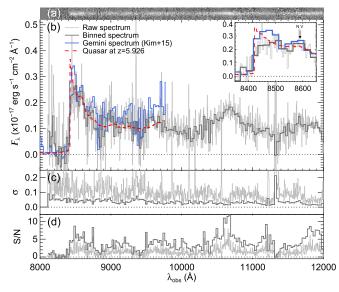
Figure 1. (a): the NIR 2D spectrum of IMS J2204+0112. (b): the NIR spectrum of IMS J2204+0112. The light gray lines represent the spectrum of IMS J2204+0112 taken with FIRE, and the dark gray lines show the spectrum binned at the spectral resolution of $R_J = 500$. The blue line represents the optical spectrum obtained with GMOS on Gemini (Kim et al. 2015). The red dashed line shows the fitted quasar model of Kim et al. (2015) with $z = 5.926$. The inset shows a zoomed-in spectrum around the Lyα break at ~8500 Å, and we marked the peak of the N V λ1240 emission line at $z = 5.926$. (c) and (d): the spectroscopic error and S/N of the NIR spectrum, respectively.

the spectrum with the most recent photometric magnitude in the z-band from the Hyper Supreme-Cam Subaru Strategic Program (HSC SSP; Aihara et al. 2018a), Data Release 1 (Aihara et al. 2018b). IMS J2204+0112 has $z = 22.55 \pm 0.05$ AB mag[11] in the HSC data, giving a flux scaling factor of 0.9. This value gives an updated M_{1450} of -23.99 ± 0.05 AB mag. The galactic extinction was corrected by the Cardelli et al. (1989) law with the extinction value A_V of ~0.127 (Schlafly & Finkbeiner 2011) assuming $R_V = 3.1$. Figure 1 shows the final spectrum of IMS J2204+0112. The uncertainty of the spectrum was derived during the aperture-extracting process.

3. Spectral Modeling

In this section, we show how we performed the spectral modeling for IMS J2204+0112 to estimate its continuum luminosity at a specific wavelength and FWHM of the C IV emission line. To use better S/N data for the spectral analysis, we binned the spectrum to match R_J (the dark gray line in Figure 1) without overlap between the pixels used for binning. Each bin contains 4–6 pixels, and we took the weighted mean of the fluxes in each bin with the weight of $w_i = \sigma_i^{-2}$, where σ_i is the error of the ith pixel in each bin. The errors in each bin (σ_{bin}) are estimated as $\sigma_{bin} = (\sum_{i=1}^{N_{pix}} w_i)^{-1/2}$, where N_{pix} is the number of pixels in each bin. We updated the wavelength calibration of the Gemini spectrum (Kim et al. 2015), and used the updated spectrum to derive redshifts, since the S/N near the

---

[11] The z'-band magnitude of IMS J2204+0112 was originally reported as 22.95 ± 0.07 AB mag (Kim et al. 2015), which is ~0.3 mag fainter than the value from the HSC data, considering the difference between z and z' filters. Note that this previous value is based on the images that were taken 9 years before the HSC data. If we use this value to normalize the spectrum, it will change λ_{Edd} by ~0.1 dex, which is negligible compared to other uncertainties in λ_{Edd} estimate.

Lyman break is about two times larger in the Gemini spectrum than the FIRE spectrum. Following the method described in Kim et al. (2015), we find the updated redshift value of $z = 5.926 \pm 0.002$ by fitting a quasar spectrum model shown as a red dashed line in Figure 1. Note that this redshift value matches the location of the peak of N V λ1240 emission line well.

3.1. Continuum Components

It is crucial for a reliable M_{BH} measurement to have a well-defined continuum model for the quasar spectrum. To increase the S/N of the continuum part of the spectrum, we binned regions with no (or weak) emission lines (e.g., 1250–1335, 1445–1495, and 1670–1690 Å) and used them (the red circles in Figure 2) to fit the continuum. Each binned point represents the weighted mean value of the specific flux density in each wavelength range. We also ignored the Fe II and Fe III lines in the continuum fitting, since they are known to be weak at $\lambda_{rest} \lesssim 2000$ Å (e.g., quasar spectra in Jiang et al. 2007; De Rosa et al. 2014).

We modeled the quasar continuum spectrum as the sum of the non-stellar power-law continuum from the accretion disk and the Balmer pseudo-continuum from gas clouds surrounding the black hole as

$$F_\lambda = F_P \left(\frac{\lambda}{1000 \text{ Å}} \right)^{\alpha_P} + F_B B_\lambda(T_e)(1 - e^{-\tau_{BE}(\lambda/\lambda_{BE})^3}),$$
$$\lambda < \lambda_{BE}, \tag{2}$$

where F_P is the normalized flux density for the non-stellar power-law continuum at 1000 Å, α_P is the slope of the power-law continuum, F_B is the normalized flux density for the Balmer continuum, $B_\lambda(T_e)$ is the Planck function at an electron temperature T_e, and τ_{BE} is the optical depth at the Balmer edge ($\lambda_{BE} = 3646$ Å in the rest-frame; Grandi 1982). Since both high- and low-redshift quasars have the slope of $\alpha_P = -1.5 \pm 1.2$ (Decarli et al. 2010; De Rosa et al. 2011; Shen et al. 2011), we adopted the fitting range of $-3.0 \leqslant \alpha_P \leqslant 1.0$, which covers 1σ dispersion of α_P. The second term is for the Balmer pseudo-continuum from Dietrich et al. (2003). The basic assumption is that there are gas clouds with uniform $T_e = 15,000$ K (Dietrich et al. 2003) in a partially optically thick condition ($\tau_{BE} = 1.0$; Kurk et al. 2007). We also tested models with $10,000 \leqslant T_e \leqslant 20,000$ K and $0.1 \leqslant \tau_{BE} \leqslant 2.0$, the range that previous studies used (e.g., De Rosa et al. 2014), but there are no significant differences between the models due to the small contribution of the Balmer continuum to the composite continuum at $\lambda_{rest} < 2000$ Å. Since our NIR spectrum does not cover the wavelength ($\lambda_{rest} = 3675$ Å) where the normalization of the model is usually done (Dietrich et al. 2003; Kurk et al. 2007; Jiang et al. 2009; De Rosa et al. 2011, 2014), we normalized the Balmer continuum with assumptions that (i) the power-law continuum is dominant at our fitting range of $1200 < \lambda_{rest} < 1800$ Å, and (ii) the flux density of the Balmer continuum can be normalized to a fraction of the power-law continuum flux density at $\lambda_{rest} = 3675$ Å that is extrapolated from our NIR data: $F_B = f_B \cdot F_P \cdot (3675 \text{ Å})^{\alpha_P}$, where f_B is the fraction of the Balmer continuum at 3675 Å. Since f_B is less than 1.0 and
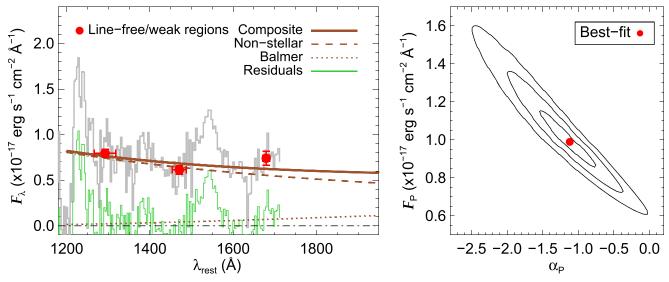
Figure 2. Left: the spectrum of IMS J2204+0112 in the rest-frame. The binned spectrum is shown as the gray line. The red circles represent the binned points of the spectrum at the line-free region. The best-fit model with the minimum $\chi^2_{\rm red}$ value is shown as the brown solid line. This model comprises the non-stellar power-law model (the brown dashed line) and the Balmer pseudo-continuum model (the brown dotted line). The residual spectrum is shown as the green line. Right: the parameter space of $\alpha_{\rm P}$ and $F_{\rm P}$ (see Section 3.1). The red dot represents our best-fit values of $\alpha_{\rm P}$ and $F_{\rm P}$, and the contours show the confidence regions (1σ to 3σ from inner to outer).

typically ~ 0.3 (Dietrich et al. 2003; De Rosa et al. 2011), the fitting range of $f_{\rm B}$ is set to $0.1 \leqslant f_{\rm B} \leqslant 1.0$.

We calculated $\chi^2_{\rm red}$ values with a grid-based parameter set of ($F_{\rm P}$, $\alpha_{\rm P}$, $f_{\rm B}$), and found the best-fit result that has the minimum $\chi^2_{\rm red}$ value, given in Table 1. The errors were computed by finding marginal points of $\chi^2_{\rm red} < \chi^2_{\rm red,min} + 1$ (1σ confidence level) in the parameter space. Figure 2 shows the best-fit continuum model plotted on the NIR spectrum of IMS J2204 +0112. The best-fit non-stellar power-law model has a slope of $\alpha_{\rm P} = -1.12^{+0.38}_{-0.40}$, consistent with that of other high-redshift quasars. For the Balmer pseudo-continuum model, the best-fit model results in $f_{\rm B} = 1.0$, due to the significant flux at ~ 1680 Å.

The flux density of the best-fit continuum model and its 1σ error are generated from the χ^2 distribution of α and $F_{\rm P}$ (Figure 2), while the other parameters ($f_{\rm B}$, T_e, and $\tau_{\rm BE}$) are fixed. From the flux density of the best-fit continuum model in the rest-frame system, we calculated the monochromatic continuum luminosity at $\lambda_{\rm rest} = 1350$ and 1450 Å (L_{1350} and L_{1450}, respectively), assuming isotropic radiation at the luminosity distance of IMS J2204+0112. We also computed the bolometric luminosity $L_{\rm bol}$ from L_{1450}, using the quasar bolometric correction from Runnoe et al. (2012): $L_{\rm bol} = 4.20 \times L_{1450}$. The estimated values with the errors at the 1σ confidence level are given in Table 2. The $\log(L_{\rm bol})$ of IMS J2204+0112 is only $46.21^{+0.12}_{-0.16}$ erg s^{-1}. Note that the errors from both the flux density and the best-fit continuum model are included in the uncertainty.

3.2. C IV Line Measurement

After subtracting the best-fit continuum model obtained from Section 3.1, we fitted the C IV emission line and measured its spectral properties. It is well-known that the C IV emission line of quasars often shows asymmetric line shapes that cannot be well modeled by a single Gaussian function (Shen et al. 2011; Tang et al. 2012; Park et al. 2013; Runnoe et al. 2013; De Rosa et al. 2014; Karouzos et al. 2015; Coatman et al. 2016; Park

Table 1
Continuum Fitting Results

Continuum Fitting Parameters	Best-fit Value with 1σ error
$F_{\rm P}$ ($\times 10^{-18}$ erg s^{-1} cm^{-2} Å^{-1})	$9.90^{+1.67}_{-1.37}$
$\alpha_{\rm P}$	$-1.12^{+0.38}_{-0.42}$
$f_{\rm B}$	$1.0^{\rm a}$
T_e (K)	$15{,}000^{\rm b}$
$\tau_{\rm BE}$	$1.0^{\rm b}$

Notes.
[a] Marginal value in the fitting range. Full details are in Section 3.1.
[b] Fixed values. Full details are in Section 3.1.

Table 2
Spectral Properties of IMS J2204+0112

Estimated Properties	Best-fit Value with 1σ error
$z^{\rm a}$	5.926 ± 0.002
$\log L_{1350}$ (erg s^{-1})	$45.59^{+0.08}_{-0.10}$
$\log L_{1450}$ (erg s^{-1})	$45.59^{+0.12}_{-0.16}$
$\log L_{\rm bol}$ (erg s^{-1})	$46.21^{+0.12}_{-0.16}$
$\lambda_{\rm C IV}$ (Å)	$1540.32^{+3.14}_{-3.20}$
FWHM$_{\rm C IV}$ (km s^{-1})	9046^{+1499}_{-1305}
$\sigma_{\rm G}$ (km s^{-1})	3841^{+636}_{-554}

Note. The uncertainties of luminosity are lower limits with constraining the contribution of the Balmer pseudo-continuum and elimination of iron lines for fitting.
[a] Derived from Gemini spectrum (Kim et al. 2015).

et al. 2017). While this asymmetric line shape of C IV can be seen in high S/N spectra (S/N $\gtrsim 10$ for continuum), it is not discernible in the spectrum with low S/N of $\lesssim 10$ (De Rosa et al. 2014), like our case. Hence, the C IV emission of IMS J2204+0112 was fitted with a single Gaussian function. For the error analysis, we adjusted the parameters of the non-stellar power-law continuum ($F_{\rm P}$ and $\alpha_{\rm P}$) using random pairs of $\alpha_{\rm P}$ and $F_{\rm P}$ following the χ^2 distribution in parameter space
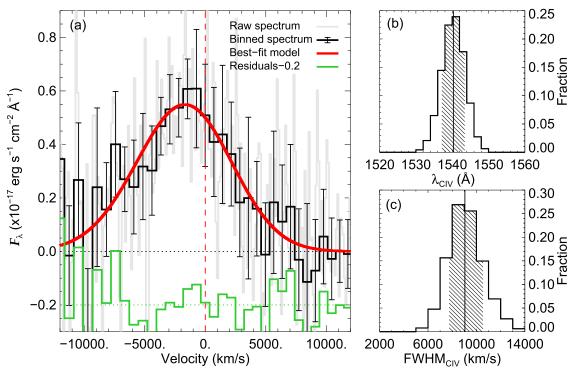
Figure 3. (a) The specific flux density of C IV emission line of IMS J2204+0112 in rest-frame after subtracting the best-fit continuum model. While the raw spectrum is shown as the gray line, the binned spectrum with flux error is shown as the black line. The red solid line represents the best-fit model for the C IV emission line, and the green line shows the residual spectrum. (b) and (c): the distributions of $\lambda_{C\,IV}$ and FWHM$_{C\,IV}$ in 100,000 trials, respectively. While the vertical line in each panel indicates the best-fit result, the shaded region corresponds to the 68% range (or 1σ confidence level) of the distribution.

(the right panel in Figure 2). This process enables us to determine the error of the continuum flux density per binned pixel. We took the quadratic sum of errors of the continuum model and of the NIR spectrum as the uncertainties of the continuum-subtracted spectrum for each pixel.

We used the MPFIT package (Markwardt 2009), a robust nonlinear least squares curve fitting with the Levenberg–Marquardt technique, for the C IV line-fitting. The fitting range was set to $1400\,\text{Å} \leqslant \lambda_{\text{rest}} \leqslant 1650\,\text{Å}$. The fitting provides the central peak wavelength $\lambda_{C\,IV}$, and the Gaussian standard deviation σ_G that is converted to the C IV line FWHM (FWHM$_{C\,IV}$) with a relation of FWHM $\simeq 2.355 \times \sigma_G$. Note that the instrumental resolution of FWHM$_{\text{ins}} = 600$ km s^{-1} is subtracted from the measured FWHM$_{\text{obs}}$ as FWHM$_{C\,IV}$ = $\sqrt{(\text{FWHM}_{\text{obs}})^2 - (\text{FWHM}_{\text{ins}})^2}$.

The panel (a) in Figure 3 shows the radial velocity profile of the C IV line. The red solid line indicates the best-fit model for the C IV emission line with $\lambda_{C\,IV} = 1540.32^{+3.14}_{-3.20}$ Å and FWHM$_{C\,IV} = 9046^{+1499}_{-1305}$ km s^{-1} (or $\sigma_G = 3841^{+636}_{-554}$ km s^{-1}). To derive the errors, we generated 100,000 mock radial profiles by adding appropriate random Gaussian noises to the best-fit model. After re-fitting the mock spectra, we took the 68% ranges of the distributions of $\lambda_{C\,IV}$ and FWHM$_{C\,IV}$ as their 1σ errors (panels (b) and (c) in Figure 3).

4. Results

4.1. Black Hole Mass

The BH mass, $M_{\text{BH,C\,IV}}$ of IMS J2204+0112 is estimated using scaling relations that utilize L_{1350} and FWHM$_{C\,IV}$

as follows:

$$\log\left(\frac{M_{\text{BH,C\,IV}}}{M_\odot}\right)$$
$$= A + \log\left\{\left(\frac{L_{1350}}{10^{44}\ \text{erg s}^{-1}}\right)^\beta \left(\frac{\text{FWHM}_{C\,IV}}{1000\ \text{km s}^{-1}}\right)^\gamma\right\}. \quad (3)$$

Many groups have suggested that one needs to be cautious about $M_{\text{BH,C\,IV}}$. The $M_{\text{BH,C\,IV}}$ values are found to have a large scatter of $\sim$0.4 dex against Hβ or Mg II-based M_{BH} values (Vestergaard & Peterson 2006; Shen et al. 2011; Ho et al. 2012; Jun et al. 2015, 2017). Also, the C IV line often shows an asymmetric shape possibly due to non-virial motion of gas and/or blending with other neighboring lines, suggesting that virial motions may not be the dominant component that determines the C IV line width. The unusual line shape is often associated with the blueshift of the C IV line, which is thought to be one of the main uncertainties in the C IV-based estimator. Several new M_{BH} estimators are derived to use blueshift as a way to improve M_{BH} measurements (Coatman et al. 2016; Jun et al. 2017). Considering these various ways of obtaining M_{BH} from the C IV line, we derived $M_{\text{BH,C\,IV}}$ using several representative estimators. Note that the virial factor of $\log f = 0.71$ (Woo et al. 2013) was used.

First, we used the estimators consistent with the idea that the exponent of the velocity term reflects the virial motion of the broad line region gas, i.e., $\gamma \sim 2$. For this, we adopted the $M_{\text{BH,C\,IV}}$ estimator of Vestergaard & Peterson (2006), Jun et al. (2015), and Park et al. (2017), where the parameter set values (A, β, γ) are (6.66, 0.53, 2.0), (6.707, 0.547, 2.11), and (6.84, 0.33, 2.00), respectively. The intrinsic scatters in the derived

Table 3
M_{BH} and λ_{Edd} of IMS J2204+0112

Reference (1)	Method (2)	$\log(M_{BH,CIV}/M_\odot)$ (3)	σ_{int} (4)	$\log \lambda_{Edd}$ (5)
Vestergaard & Peterson (2006)[a]	$\gamma = 2$	$9.38^{+0.13}_{-0.15}$	0.36	-1.27
Jun et al. (2015)	$\gamma = 2$	$9.55^{+0.24}_{-0.24}$	0.40	-1.43
Park et al. (2017)	$\gamma = 2$	$9.27^{+0.19}_{-0.20}$	0.22	-1.16
Park et al. (2017)[a]	$\gamma = 0.50$	$8.72^{+0.60}_{-0.59}$	0.16	-0.61
Coatman et al. (2017)[a]	$v_{bs,CIV}$[b]	$9.05^{+0.26}_{-0.29}$	~ 0.5	-0.93
Jun et al. (2017)	$v_{bs,CIV}$[b]	$9.27^{+0.27}_{-0.28}$	~ 0.35	-1.15
Park et al. (2017)[a]	σ_{CIV}	$8.59^{+0.19}_{-0.21}$	0.12	-0.48
Park et al. (2017)	σ_G	$8.58^{+0.18}_{-0.19}$	0.12	-0.47
Weighted mean	⋯	9.09 ± 0.41	⋯	-0.97

Notes. The results of $M_{BH,CIV}$ and λ_{Edd} measurements from several methods. Column 1: references. Column 2: methods for $M_{BH,CIV}$ estimation. Column 3: $M_{BH,CIV}$ with 1σ errors. The intrinsic scatter of each method is not included in the error. Column 4: intrinsic scatter of the M_{BH} estimator. Column 5: λ_{Edd}.
[a] The methods used for calculating the weighted mean M_{BH} value with the weight of the inverse variance of the M_{BH} estimates.
[b] The $v_{bs,CIV}$ value used in this method is derived from the continuum break and the N V line, and this procedure could bias the result.

M_{BH} are of the order of ± 0.3 dex in these estimators (see Table 3). Using the line luminosity and FWHM values we obtained in Section 3, we find that the $M_{BH,CIV}$ values of IMS J2204+0112 are $\log(M_{BH,CIV}/M_\odot) = 9.38^{+0.13}_{-0.15}$ (Vestergaard & Peterson 2006), $9.55^{+0.24}_{-0.24}$ (Jun et al. 2015), and $9.27^{+0.19}_{-0.20}$ (Park et al. 2017). The 1σ uncertainty of $M_{BH,CIV}$ is estimated by inserting the rms uncertainties of L_{1350} and FWHM$_{CIV}$ in the M_{BH} estimators. All three estimators give values that are consistent within error, with $\log(M_{BH,CIV}/M_\odot) \sim 9.4$.

Second, we used the estimator with a very small γ value of ~ 0.5, which is not consistent with the virial motion assumption. This kind of estimator is put forward to minimize the scatter in M_{BH} between this method and the reverberation mapping result. Using the relation that adopts a parameter set of (7.54, 0.45, 0.5) from Park et al. (2017), we find $\log(M_{BH,CIV}/M_\odot) = 8.72^{+0.60}_{-0.59}$, with an intrinsic scatter of 0.16 dex. This is about 0.6 dex smaller than the nominal M_{BH} estimates above, but showing very large uncertainty due to a γ of $0.50^{+0.55}_{-0.53}$. However, the adoption of the low γ value may not be physically plausible (Denney et al. 2013), and Jun et al. (2015) have shown that such a relation is likely to underestimate/overestimate M_{BH} at the high ($\log(M_{BH}/M_\odot) > 9.5$) and low mass ends ($\log(M_{BH}/M_\odot) < 8$).

Third, we used the estimators that correct the blueshift effect of the C IV line, since the blueshift of the C IV line ($v_{bs,CIV} \equiv c \times (1549.48 - \lambda_{CIV})/1549.48$) can be a signal to correct possible bias in $M_{BH,CIV}$ (Coatman et al. 2016, 2017; Jun et al. 2017). Using the λ_{CIV} value from Section 3.2 and the systemic redshift of $z = 5.926$, we estimate the C IV blueshift as $v_{bs,CIV} = 1685^{+608}_{-620}$ km s^{-1}. Using either the parameter set of (6.71, 0.53, 2) in Equation (6) of Coatman et al. (2017) or $M_{BH,CIV}$ with the blueshift correction term of Jun et al. (2017), we get $\log(M_{BH,CIV}/M_\odot) = 9.05^{+0.26}_{-0.29}$, and $\log(M_{BH,CIV}/M_\odot) = 9.27^{+0.27}_{-0.28}$, respectively. These values are consistent within the error. Note that the systemic redshift of IMS J2204+0112 is derived from the continuum break and the location of the N V line; we assume that this is identical to the redshift derived

from a narrow high ionization line (e.g., [O III]), or host galaxy emission (e.g., Far-infrared [C II]). If this assumption is wrong, the derived M_{BH} with this method could be biased. Furthermore, the Mg II line of a few high-redshift quasars is statistically blueshifted compared to CO and [C II] emission lines, while that of low-redshift ones is not (Venemans et al. 2016; Mazzucchelli et al. 2017). These imply that the application of the blueshift correction factor from the $z < 4$ quasars may be inappropriate for high-redshift quasars.

An alternative way to derive $M_{BH,CIV}$ is to use the line dispersion of the C IV line (σ_{CIV}; Denney et al. 2013; Park et al. 2013, 2017). The second moment line dispersion σ_{CIV} is $\sim 3900 \pm 700$ km s^{-1}, which is calculated within ± 10000 km s^{-1} around λ_{CIV}. With the best-fit parameter set from Park et al. (2017), this σ_{CIV} and the σ_G (estimated in Section 3.2) give $\log(M_{BH,CIV}/M_\odot) = 8.59^{+0.19}_{-0.21}$ and $8.58^{+0.18}_{-0.19}$, respectively. But the σ_{CIV} value varies significantly with the fitting range due to the low S/N of the continuum, as also noticed in previous studies (Denney et al. 2013; Coatman et al. 2016). Furthermore, $M_{BH,CIV}$ with σ_G being possibly underestimated considering the common shape of the C IV line (Denney et al. 2013; Park et al. 2013, 2017).

In Table 3, we list these $M_{BH,CIV}$ values of IMS 2204+0112. As a representative M_{BH} value, we use the weighted mean of the M_{BH} value ($\log(M_{BH,CIV}/M_\odot) = 9.09 \pm 0.41$) from different methods; $\gamma = 2$ (Vestergaard & Peterson 2006), $\gamma = 0.5$ (Park et al. 2017), $v_{bs,CIV}$ (Coatman et al. 2017), and σ_{CIV} (Park et al. 2017). Note that the weight is the inverse variance of the M_{BH} estimation in each method. Not surprisingly, this value matches closely with the M_{BH} value from Mg II of lower-redshift quasars with spectral characteristics similar to IMS J2204+0112.[12]

4.2. Eddington Ratio

Using the $M_{BH,CIV}$ and L_{bol} values from previous sections, we calculate $\lambda_{Edd} = L_{bol}/L_{Edd}$. The calculated λ_{Edd} values are listed in Table 3, indicating that λ_{Edd} is 0.10, one of the lowest values among quasars at $z \sim 6$.

Figure 4 shows L_{bol} versus the M_{BH} of IMS J2204+0112 (the red diamond; weighted mean $M_{BH,CIV}$ value), quasars at $z \sim 6$ (the navy diamonds), and at $z < 3$ (the gray dots and contours). In the left panel, we show the values that are based on $M_{BH,CIV}$ from the Vestergaard & Peterson (2006) relation, and in the right panel, the Mg II-based M_{BH} values, $M_{BH,MgII}$ (Vestergaard & Osmer 2009), are given. The L_{bol} and M_{BH} values of $z \sim 6$ quasars are derived in the same manner as done for IMS J2204+0112 using the literature values of L_{1350} and FWHM$_{CIV}$ (Jiang et al. 2007; Kurk et al. 2007) or L_{3000} and FWHM$_{MgII}$ (Willott et al. 2003, 2010a; Kurk et al. 2007, 2009; De Rosa et al. 2011; Wu et al. 2015). For quasars at $z < 3$, we take the values from Shen et al. (2011), where the $M_{BH,CIV}$ values are based on the Vestergaard & Peterson (2006) relation and the $M_{BH,MgII}$ values are derived using the Vestergaard & Osmer (2009) relation.

The striking feature in the figure is that IMS J2204+0112 occupies a unique parameter space, the parameter space that has not been populated by other $z = 6$ luminous quasars, but is

---

[12] One can also adopt the M_{BH} derived from Mg II estimators of quasars that have spectral properties similar to IMS J2204+0112. For this, we selected quasars with $7500 <$ FWHM$_{CIV}$ (km s^{-1}) $< 10,500$, and $45 < \log L_{1350}$ (erg s^{-1}) < 46 from Shen et al. (2011) and obtained their mean M_{BH} from Mg II. We obtain $\log(M_{BH,MgII}/M_\odot) = 9.08 \pm 0.40$.
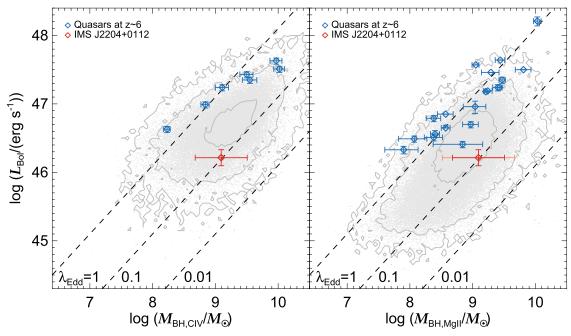
Figure 4. M_{BH}–L_{bol} distributions of quasars. The left and the right panels show the results based on $M_{BH,C\,IV}$ and $M_{BH,Mg\,II}$, respectively. While the gray dots and the contours represent the low-redshift quasars from SDSS DR7 Quasar catalog (Shen et al. 2011), the blue diamonds indicate quasars at $z \sim 6$ (Jiang et al. 2007; Kurk et al. 2007, 2009; Willott et al. 2010a; De Rosa et al. 2011; Wu et al. 2015). IMS J2204+0112 is shown as the red diamond, which seems to be isolated from other high-redshift quasars. Note that the red error bar of IMS J2204+0112 in the right panel includes the error of M_{BH} measurements and the dispersion of $M_{BH,Mg\,II}$ compared to $M_{BH,C\,IV}$. This figure indicates that IMS J2204+0112 is a quasar with an exceptionally low λ_{Edd} among $z = 6$ quasars.

rather common among $z \sim 2$ quasars. This prompts a question: have we only been seeing a limited population of high λ_{Edd} quasars in previous studies? If we impose the survey depth of IMS of $J_{AB} < 22.5$–23.0 mag (Kim et al. 2015) for the intrinsic λ_{Edd} distribution from Willott et al. (2010a), the λ_{Edd} distribution for such a magnitude-limited survey has a peak value at $\log \lambda_{Edd} = -0.10$ and a dispersion of 0.26 dex. In such a case, there is only a chance of $\sim 0.03\%$ (or 3.5σ away from the peak) of finding a quasar with a λ_{Edd} lower than IMS J2204+0112. Even if we consider the 1σ error of λ_{Edd} of IMS J2204+0112 ($\log \lambda_{Edd} = -0.56$), the probability is only 3.84%, which is still low. That is to say, the probability of finding such a quasar in IMS is quite low for the intrinsic λ_{Edd} distribution of Willott et al. (2010a).

5. Discussion

It is remarkable that there is a faint quasar with only $\lambda_{Edd} = 0.10$ at $z \sim 6$, though its mass determination is quite uncertain due to the characteristics of the C IV line. Recently, it was suggested that the average λ_{Edd} of high-redshift quasars is similar to that of their luminosity-matched counterparts at low redshift (Mazzucchelli et al. 2017). The existence of IMS J2204+0112 reinforces that suggestion even at a lower L_{bol} of $\sim 10^{46}$ erg s^{-1}.

As we mentioned in the introduction, the growth of a $100\,M_\odot$ seed BH to a $\sim 10^9\,M_\odot$ SMBH at $z = 6$ is already very challenging due to the short time available between the creation of the BH seed and the epoch of $z = 6$. The situation gets significantly worse if $\lambda_{Edd} = 0.10$. At $\lambda_{Edd} = 0.10$, Equation (1) shows that it takes 8 Gyr to obtain a $10^9\,M_\odot$ BH from a stellar-mass seed. Therefore, in such a case, it is impossible to grow stellar-mass BHs into SMBHs in quasars at $z \sim 6$. Thus, alternative scenarios must be sought if the λ_{Edd} value is around 0.10 for IMS J2204+0112 at $z \sim 6$.

Recent studies promote super-Eddington accretion as a way to create $10^9\,M_\odot$ BHs by $z = 6$. In that scenario, episodes of short-duration or steady super-Eddington accretion are shown to create SMBHs by $z = 6$, with a duty cycle of 0.5 or less (Li 2012; Madau et al. 2014; Smole et al. 2015; Volonteri et al. 2015; Pezzulli et al. 2016; Sakurai et al. 2016; De Graf et al. 2017). In the case of super-Eddington accretion with a slim disk (Watarai et al. 2001; Wang & Netzer 2003; Ohsuga et al. 2005; Volonteri et al. 2015), $\dot{m}$ in Equation (1) is given by

$$\dot{m} \sim \frac{2}{\epsilon} \exp\left(\frac{\lambda_{Edd}}{2} - 1\right), \qquad (4)$$

for $\lambda_{Edd} \geqslant 2$. For example, if we have a super-Eddington accretion with $\lambda_{Edd} = 3$, adopting $\epsilon \sim 0.04$ (Mineshige et al. 2000) with a duty cycle of $f_{Duty} = 0.5$, only about 180 Myr is needed to create a $10^9\,M_\odot$ BH from a $10^2\,M_\odot$ seed BH, while the SMBH can have a low λ_{Edd} (~ 0.1 or less) for the remaining time (see also Trakhtenbrot et al. 2017). Under the episodic super-Eddington accretion scenario with a stellar-mass seed BH, our result of $\lambda_{Edd} = 0.1$ implies that IMS J2204+0112 underwent bursts of super-Eddington accretion before, and is relatively quiescent at $z \sim 6$.

Another possible BH growth scenario is to have very heavy seed BHs with $M_{BH,0} \sim 10^4$–$10^6\,M_\odot$ (Volonteri et al. 2008; De Graf et al. 2012; Di Matteo et al. 2012; Johnson et al. 2013, 2013; Ferrara et al. 2014; Pacucci et al. 2015; Gallerani et al. 2017; Regan et al. 2017; Smidt et al. 2017 and references therein). Using Equation (1) with the final BH mass of $M_{BH} = 10^9\,M_\odot$, and $M_{BH,0} = 10^5\,M_{BH}$ for the seed BH, we get the accretion timescale of ~ 4.6 Gyr if the accretion continues at $\lambda_{Edd} = 0.10$ and ~ 0.46 Gyr at $\lambda_{Edd} = 1$. Therefore, a $10^5\,M_\odot$ seed BH can become a $10^9\,M_\odot$ BH if the BH growth can last about a few hundred Myr at the Eddington limit before

subsiding to $\lambda_{\mathrm{Edd}} \sim 0.1$ at $z = 6$. Simulations show that cold gas flows can feed massive BH seeds (De Graf et al. 2012; Di Matteo et al. 2012; Smidt et al. 2017). In the simulation, the BH growth proceeds nearly at Eddington-limited accretion for an extended period until $z \sim 7$ or so and then reduces to $\lambda_{\mathrm{Edd}} \sim 0.1$ or less (e.g., Di Matteo et al. 2012; Smidt et al. 2017). This is consistent with our findings.

6. Conclusion

Through deep NIR spectroscopic observations using FIRE on the Magellan telescope, we measured the M_{BH} and λ_{Edd} of one of the faintest quasars at $z \sim 6$. Our result shows that IMS J2204+0112 has $M_{\mathrm{BH}} \sim 10^9 M_{\odot}$ and a relatively low Eddington ratio of $\lambda_{\mathrm{Edd}} = 0.1$ in comparison to other $z = 6$ quasars, implying that IMS J2204+0112 is a mature SMBH at high redshift with two possible growth scenarios: BH growth from a massive seed BH ($\sim 10^5 M_{\odot}$), or BH growth through short, episodic super-Eddington accretion of stellar-mass BHs. The rather low λ_{Edd} of IMS J2204+0112 is in line with the recent report that the average λ_{Edd} of high-redshift quasars could be similar to that of lower-redshift quasars (Mazzucchelli et al. 2017). The reliability of the M_{BH} measurements can be improved by observing the Mg II line or the Balmer lines, and the λ_{Edd} measurements can be improved with multi-wavelength observations that include longer wavelengths (e.g., submm). Upcoming extremely large telescopes, such as the Giant Magellan Telescope and the *James-Webb Space Telescope*, will allow us to routinely observe faint quasars to measure M_{BH} reliably, giving a vivid perspective on SMBH evolution in the early universe.

ORCID iDs

Yongjung Kim ⓘ https://orcid.org/0000-0003-1647-3286
Myungshin Im ⓘ https://orcid.org/0000-0002-8537-6714
Yiseul Jeon ⓘ https://orcid.org/0000-0003-4847-7492
Minjin Kim ⓘ https://orcid.org/0000-0002-3560-0781
Jae-Woo Kim ⓘ https://orcid.org/0000-0002-1710-4442
Hyunsung David Jun ⓘ https://orcid.org/0000-0003-1470-5901
Marios Karouzos ⓘ https://orcid.org/0000-0002-8858-3188
Duho Kim ⓘ https://orcid.org/0000-0001-5120-0158
Ji Hoon Kim ⓘ https://orcid.org/0000-0002-1418-3309
Seong-Kook Lee ⓘ https://orcid.org/0000-0001-5342-8906
Soojong Pak ⓘ https://orcid.org/0000-0002-2548-238X

References

Aihara, H., Arimoto, N., Armstrong, R., et al. 2018a, PASJ, 70, S4
Aihara, H., Armstrong, R., Bickerton, S., et al. 2018b, PASJ, 70, S8
Alexander, D. M., & Hickox, R. C. 2012, NewAR, 56, 93
Alvarez, M. A., Wise, J. H., & Abel, T. 2009, ApJL, 701, L133
Bañados, E., Venemans, B. P., Decarli, R., et al. 2016, ApJS, 227, 11
Bañados, E., Venemans, B. P., Mazzucchelli, C., et al. 2018, Natur, 553, 473
Bañados, E., Venemans, B. P., Morganson, E., et al. 2014, AJ, 148, 14
Begelman, M. C., Volonteri, M., & Rees, M. J. 2006, MNRAS, 370, 289
Boyle, B. J., Shanks, T., Croom, S. M., et al. 2000, MNRAS, 317, 1014
Bromm, V., & Loeb, A. 2003, ApJL, 596, L34
Cardelli, J. A., Clayton, G. C., & Mathis, J. S. 1989, ApJ, 345, 245
Coatman, L., Hewett, P. C., Banerji, M., et al. 2017, MNRAS, 465, 2120
Coatman, L., Hewett, P. C., Banerji, M., & Richards, G. T. 2016, MNRAS, 461, 647
De Graf, C., Dekel, A., Gabor, J., & Bournaud, F. 2017, MNRAS, 466, 1462
De Graf, C., Di Matteo, T., Khandai, N., et al. 2012, MNRAS, 424, 1892
Decarli, R., Falomo, R., Treves, A., et al. 2010, MNRAS, 402, 2453
Denney, K. D., Pogge, R. W., Assef, R. J., et al. 2013, ApJ, 775, 60
De Rosa, G., Decarli, R., Walter, F., et al. 2011, ApJ, 739, 56
De Rosa, G., Venemans, B. P., Decarli, R., et al. 2014, ApJ, 790, 145
Dietrich, M., Hamann, F., Appenzeller, I., & Vestergaard, M. 2003, ApJ, 596, 817
Di Matteo, T., Khandai, N., DeGraf, C., et al. 2012, ApJL, 745, L29
Fan, X., Strauss, M. A., Becker, R. H., et al. 2006, AJ, 132, 117
Fan, X., White, R. L., Davis, M., et al. 2000, AJ, 120, 1167
Ferrara, A., Salvadori, S., Yue, B., & Schleicher, D. 2014, MNRAS, 443, 2410
Flesch, E. W. 2015, PASA, 32, 10
Gallerani, S., Fan, X., Maiolino, R., & Pacucci, F. 2017, PASA, 34, e022
Giallongo, E., Grazian, A., Fiore, F., et al. 2015, A&A, 578, A83
Goto, T. 2006, MNRAS, 371, 769
Grandi, S. A. 1982, ApJ, 255, 25
Hewett, P. C., Foltz, C. B., & Chaffee, F. H. 1995, AJ, 109, 1498
Ho, L. C., Goldoni, P., Dong, X.-B., Greene, J. E., & Ponti, G. 2012, ApJ, 754, 11
Im, M., Griffiths, R. E., & Ratnatunga, K. U. 1997, ApJ, 475, 457
Im, M., Lee, I., CHo, Y., et al. 2007, ApJ, 664, 64
Jeon, M., Pawlik, A. H., Greif, T. H., et al. 2012, ApJ, 754, 34
Jeon, Y., Im, M., Kim, D., et al. 2017, ApJS, 231, 16
Jiang, L., Fan, X., Bian, F., et al. 2009, AJ, 138, 305
Jiang, L., Fan, X., Brandt, W. N., et al. 2010, Natur, 464, 380
Jiang, L., Fan, X., Vestergaard, M., et al. 2007, AJ, 134, 1150
Jiang, L., McGreer, I. D., Fan, X., et al. 2016, ApJ, 833, 222
Johnson, J. L., Whalen, D. J., Li, H., & Holz, D. E. 2013, ApJ, 771, 116
Jun, H. D., & Im, M. 2013, ApJ, 779, 104
Jun, H. D., Im, M., Kim, D., & Stern, D. 2017, ApJ, 838, 41
Jun, H. D., Im, M., Lee, H. M., et al. 2015, ApJ, 806, 109
Karouzos, M., Woo, J.-H., Matsuoka, K., et al. 2015, ApJ, 815, 128
Kashikawa, N., Ishizaki, Y., Willott, C. J., et al. 2015, ApJ, 798, 28
Kim, D., Im, M., & Kim, M. 2010, ApJ, 724, 386
Kim, Y., Im, M., Jeon, Y., et al. 2015, ApJL, 813, L35
Kurk, J. D., Walter, F., Fan, X., et al. 2007, ApJ, 669, 32
Kurk, J. D., Walter, F., Fan, X., et al. 2009, ApJ, 702, 833
Lee, I., Im, M., Kim, M., et al. 2008, ApJS, 175, 116
Li, L.-X. 2012, MNRAS, 424, 1461
Lodato, G., & Natarajan, P. 2006, MNRAS, 371, 1813
Lusso, E., Comastri, A., Simmons, B. D., et al. 2012, MNRAS, 425, 623
Madau, P., Haardt, F., & Dotti, M. 2014, ApJL, 784, L38
Markwardt, C. B. 2009, adass XVIII, 411, 251
Matsuoka, Y., Onoue, M., Kashikawa, N., et al. 2016, ApJ, 828, 26
Matsuoka, Y., Onoue, M., Kashikawa, N., et al. 2018, PASJ, 70, S35

Mazzucchelli, C., Bañados, E., Venemans, B. P., et al. 2017, ApJ, 849, 91
Milosavljević, M., Couch, S. M., & Bromm, V. 2009, ApJL, 696, L146
Mineshige, S., Kawaguchi, T., Takeuchi, M., & Hayashida, K. 2000, PASJ, 52, 499
Mortlock, D. J., Warren, S. J., Venemans, B. P., et al. 2011, Natur, 474, 616
Ohsuga, K., Mori, M., Nakamoto, T., & Mineshige, S. 2005, ApJ, 628, 368
Pacucci, F., Volonteri, M., & Ferrara, A. 2015, MNRAS, 452, 1922
Pâris, I., Petitjean, P., Ross, N. P., et al. 2017, A&A, 597, A79
Park, D., Barth, A. J., Woo, J.-H., et al. 2017, ApJ, 839, 93
Park, D., Woo, J.-H., Denney, K. D., & Shin, J. 2013, ApJ, 770, 87
Park, K., & Ricotti, M. 2012, ApJ, 747, 9
Pelupessy, F. I., Di Matteo, T., & Ciardi, B. 2007, ApJ, 665, 107
Pezzulli, E., Valiante, R., & Schneider, R. 2016, MNRAS, 458, 3047
Regan, J. A., Visbal, E., Wise, J. H., et al. 2017, NatAs, 1, 0075
Richards, G. T., Strauss, M. A., Fan, X., et al. 2006, AJ, 131, 2766
Runnoe, J. C., Brotherton, M. S., & Shang, Z. 2012, MNRAS, 422, 478
Runnoe, J. C., Brotherton, M. S., Shang, Z., & DiPompeo, M. A. 2013, MNRAS, 434, 848
Sakurai, Y., Inayoshi, K., & Haiman, Z. 2016, MNRAS, 461, 4496
Schlafly, E. F., & Finkbeiner, D. P. 2011, ApJ, 737, 103
Schmidt, M., & Green, R. F. 1983, ApJ, 269, 352
Shen, Y., Greene, J. E., Strauss, M. A., Richards, G. T., & Schneider, D. P. 2008, ApJ, 680, 169
Shen, Y., Richards, G. T., Strauss, M. A., et al. 2011, ApJS, 194, 45
Smidt, J., Whalen, D. J., Johnson, J. L., & Li, H. 2017, arXiv:1703.00449

Smole, M., Micic, M., & Martinović, N. 2015, MNRAS, 451, 1964
Tang, B., Shang, Z., Gu, Q., Brotherton, M. S., & Runnoe, J. C. 2012, ApJS, 201, 38
Tody, D. 1993, adass II, 52, 173
Trakhtenbrot, B., & Netzer, H. 2012, MNRAS, 427, 3081
Trakhtenbrot, B., Volonteri, M., & Natarajan, P. 2017, ApJL, 836, L1
Venemans, B. P., Bañados, E., Decarli, R., et al. 2015a, ApJL, 801, L11
Venemans, B. P., Findlay, J. R., Sutherland, W. J., et al. 2013, ApJ, 779, 24
Venemans, B. P., Verdoes Kleijn, G. A., Mwebaze, J., et al. 2015b, MNRAS, 453, 2259
Venemans, B. P., Walter, F., Zschaechner, L., et al. 2016, ApJ, 816, 37
Vestergaard, M., & Osmer, P. S. 2009, ApJ, 699, 800
Vestergaard, M., & Peterson, B. M. 2006, ApJ, 641, 689
Volonteri, M. 2012, Sci, 337, 544
Volonteri, M., Lodato, G., & Natarajan, P. 2008, MNRAS, 383, 1079
Volonteri, M., & Rees, M. J. 2005, ApJ, 633, 624
Volonteri, M., Silk, J., & Dubus, G. 2015, ApJ, 804, 148
Wang, J.-M., & Netzer, H. 2003, A&A, 398, 927
Watarai, K.-y., Mizuno, T., & Mineshige, S. 2001, ApJL, 549, L77
Willott, C. J., Albert, L., Arzoumanian, D., et al. 2010a, AJ, 140, 546
Willott, C. J., Delorme, P., Reylé, C., et al. 2010b, AJ, 139, 906
Willott, C. J., McLure, R. J., & Jarvis, M. J. 2003, ApJL, 587, L15
Woo, J.-H., Schulze, A., Park, D., et al. 2013, ApJ, 772, 49
Wu, X.-B., Wang, F., Fan, X., et al. 2015, Natur, 518, 512
Wyithe, J. S. B., & Loeb, A. 2012, MNRAS, 425, 2892